

# Flow Separation Control Using Nanosecond Pulse Driven DBD Plasma Actuators

Chris Rethmel, Jesse Little<sup>1</sup>, Keisuke Takashima, Aniruddha Sinha<sup>2</sup>,  
Igor Adamovich and Mo Samimy\*

Department of Mechanical and Aerospace Engineering, The Ohio State University, 2300  
West Case Road, Columbus, Ohio 43235-7531, USA

[Received date; Accepted date]

## ABSTRACT

This work continues an ongoing effort aimed at development and use of dielectric barrier discharge (DBD) plasma actuators driven by repetitive nanosecond pulses for high Reynolds number aerodynamic flow control. These actuators are believed to influence the flow via a thermal mechanism which is fundamentally different from more commonly studied AC-DBD actuators. Leading edge separation control on an 8-inch chord NACA 0015 airfoil is demonstrated at various post-stall angles of attack for Mach numbers up to 0.26 (free stream velocity up to 93 m/s) and Reynolds numbers up to  $1.15 \times 10^6$ . The nanosecond (NS) pulse driven DBD is shown to extend the stall angle at low Reynolds numbers by functioning as an active trip. At post-stall angles of attack, the device is shown to excite shear layer instabilities and generate coherent spanwise vortices that transfer momentum from the freestream to the separated region, thus reattaching the flow. This is observed for all high Reynolds numbers and Mach numbers spanning the speed range of the subsonic tunnel used in this work. A comparison of leading edge separation control between NS-DBD and AC-DBD plasma actuation demonstrates the increased control authority of NS-DBD plasma at higher flow speeds. The NS-DBD actuator is also integrated into a feedback control system with a stagnation-line-sensing hot film. A simple on/off type controller is developed that operates based on a threshold of the power dissipated by the hot film. An extremum seeking controller is also investigated for dynamically varying  $Re$ . Several challenges typically associated with the integration of DBD plasma actuators into a feedback control system have been overcome. The most important of these is the demonstration of control authority at typical aircraft takeoff and landing Mach numbers.

## 1. INTRODUCTION

Flow separation control with periodic excitation is widely established as a successful actuation technique in many flow systems (Greenblatt and Wygnanski 2000). This active flow control technology has the potential to substantially decrease the manufacturing cost, weight and parasitic drag associated with many passive control systems that rely purely on geometric modifications to the aerodynamic surface (McLean *et al.* 1999). Practical active flow control systems should incorporate feedback for robust operation in the presence of uncertainties, and successful implementations have been demonstrated in various aerodynamic systems (Becker *et al.* 2007; Patel *et al.* 2007; Pinier *et al.* 2007; Samimy *et al.* 2007; Benard *et al.* 2010b; Poggie *et al.* 2010; Sinha *et al.* 2010).

The periodic excitation used for active flow control is often generated using oscillatory momentum devices that produce zero-net mass flux (Glezer and Amitay 2002). The optimal dimensionless frequency,  $F^+ = fx_{sep}/U_\infty$ , for controlling separation using periodic excitation is on the order of unity where  $f$ ,  $x_{sep}$  and  $U_\infty$  are the forcing frequency, separation length scale, and freestream velocity, respectively (Seifert *et al.* 1996). This provides some guidance for selecting optimal frequencies, but is by no means a universal optimum. Momentum can be introduced by a variety of techniques, but the most

1. Currently, Department of Aerospace and Mechanical Engineering, University of Arizona, Tucson

\*Corresponding author; E-mail: samimy.1@osu.edu

2 Currently, California Institute of Technology, Pasadena

common are piezoelectric, electromagnetic and electrostatic. In all of these cases, an electromechanical driver creates the oscillatory flow used for excitation. These devices are controlled through electrical signals and, compared to passive control, offer a significant reduction in weight, mechanical complexity and parasitic drag. Unfortunately, they possess limited bandwidth and are subject to mechanical failure because the electromechanical driver is usually operated at resonance to produce the large amplitude perturbations necessary for realizing control authority at practical flight speeds. Even when operated in this fashion, it is difficult to meet amplitude requirements especially for cruise conditions since the required actuator momentum scales roughly with dynamic pressure (Greenblatt and Wygnanski, 2000).

Flow control with plasma actuation is appealing because these devices are entirely surface mounted, lack mechanical parts, and can possess high bandwidth while requiring relatively low power. Dielectric Barrier Discharge (DBD) plasma actuators driven by AC waveforms (AC-DBD) are the most commonly used of these devices (Corke *et al.* 2009). They have been widely studied for controlling flow separation, particularly on the leading edge of airfoils at  $Re \sim 10^5$  and  $U_\infty \sim 30$  m/s (Moreau 2007), but only a few demonstrations of this technology exist at higher  $Re$  and  $M$  (see Kelley *et al.*, 2012). The control mechanism for AC-DBD plasma actuators arises from an electrohydrodynamic (EHD) effect. Collisions between the charged species in the plasma and neutral particles near the surface generate a low speed (usually  $< 10$  m/s) near-wall jet in quiescent air (Forte *et al.* 2007). The momentum production of these devices is fundamentally restricted by ion density in the space-charge region of electric discharge (Macheret *et al.* 2004), which has limited their use at higher speeds, although continuous improvements are being made (Thomas *et al.* 2009; Kelley *et al.*, 2012).

Early reports suggest DBD plasma actuators driven by a different type of waveform could be a good alternative (Roupassov *et al.* 2009). The construction of the device is analogous to the AC-DBD, but the discharge is driven by repetitive nanosecond duration pulses with full width at half max (FWHM) of 5–100 ns. We will refer to this type of actuation as a repetitive nanosecond pulse discharge or “NS-DBD” throughout the paper. DBD plasma created using these waveforms has shown control authority for airfoil separation control up to transonic speed (Roupassov *et al.* 2009). The NS-DBD produces very low velocity in the neutral species and the control mechanism is believed to stem from rapid localized heating of the near surface gas layer (Roupassov *et al.* 2009; Little *et al.* 2012). This mechanism is well-established for localized arc filament plasma actuators (LAFPA) that have demonstrated control authority in high Reynolds number and high-speed (subsonic/supersonic, cold/hot) jets in both experiments (Samimy *et al.* 2010) and computations (Gaitonde and Samimy 2011).

This work continues further exploration of the use of dielectric barrier discharge plasma actuators driven by repetitive nanosecond pulses for aerodynamic flow control. The efficacy of NS-DBD pulses has previously been demonstrated on an airfoil leading edge up to  $Re = 1 \times 10^6$  (62 m/sec) (Little *et al.* 2012). The current work extends the investigation to higher  $M$  (0.26, 93 m/s) and  $Re$  ( $1.15 \times 10^6$ ) using an 8 inch chord NACA 0015 airfoil commonly studied with active flow control. It also incorporates an actuator recessed in the airfoil surface which reduces discontinuities near the leading edge. The NS-DBD actuator is integrated into a feedback control system with stagnation-line-sensing hot films near the leading edge. These sensors can be used to identify critical points and have recently been implemented in AC-DBD plasma feedback control studies of lift enhancement (Poggie *et al.* 2010). Two types of control systems are investigated. The first is a very simple on/off type controller that operates based on a mean hot film signal value threshold for static  $Re$  conditions. The second is an extremum-seeking controller that is tested by dynamically varying the Reynolds number. The practical utility of these feedback controllers is not fully realized, due to the unfavorable location of the sensor. However, several of the challenges typically associated with DBD plasma actuators have been overcome. The most important of these is the demonstration of control authority at  $Re > 10^6$  and  $M > 0.25$  which represent the maximum conditions available in the experimental test bed. Many remaining challenges are currently being addressed.

## 2. EXPERIMENTAL FACILITIES AND TECHNIQUES

### 2.1. Wind Tunnel Facility and Airfoil Model

All the experiments are performed in a closed, recirculating wind tunnel at the OSU Gas Dynamics and Turbulence Laboratory that produces velocities of 3–95 m/s with free stream turbulence levels on the order of 0.25%. The tunnel has a test section of  $61 \times 61 \times 122$  cm<sup>3</sup> ( $2 \times 2 \times 4$  ft<sup>3</sup>) and includes a heat exchanger to regulate the flow temperature. The operating conditions of the tunnel are measured using static pressure taps at the inlet and exit of the contraction section with two sets of differential pressure

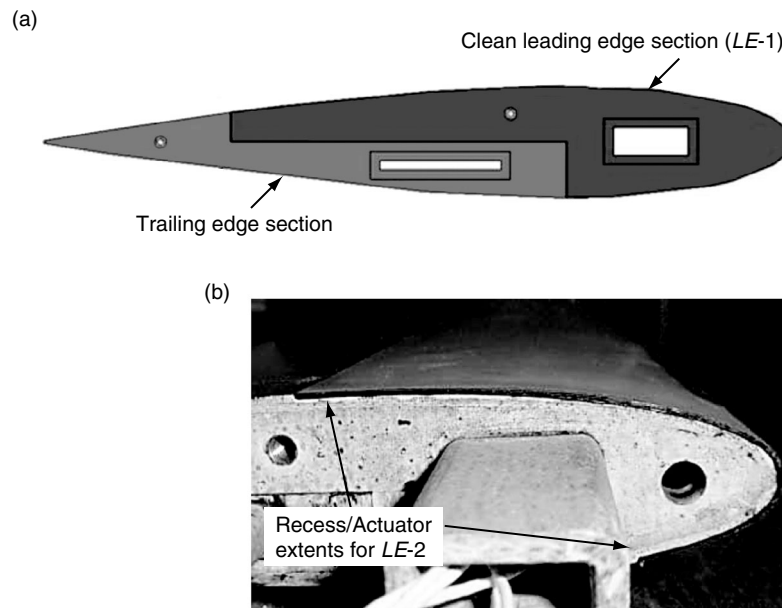


Figure 1. Schematic of two-section baseline airfoil, *LE-1* (a) and photograph of airfoil with actuator installed in leading edge recess, *LE-2* (b).

transducers (Omega Engineering, Inc. PX655-25DI and PX655-5DI). The pressure measurements are displayed and acquired by the data acquisition system using two process meters (Omega Engineering, Inc. DP-25-E-A).

The model used in these experiments is a NACA 0015 airfoil with a chord length of 20.32 cm (8 in) and a span of 61 cm (2 ft). The fiberglass model consists of two separate pieces; a trailing edge section and an interchangeable leading edge section (Figure 1). The seams produced by mating the forward and aft pieces have been located at  $x/c = 75\%$  on the suction side and  $x/c = 30\%$  on the pressure side to avoid disturbing the developing boundary layer near the leading edge (*LE*). Each piece of the model has a hollow spar that serves as a support structure and also allows vinyl tubing used in  $C_p$  measurements to exit the model. One leading edge section (*LE-1*), designed per the standard NACA 0015 profile, provides baseline performance data. A second leading edge section is constructed with a 0.76 mm (30 mil) recess wrapping around the leading edge from 10% chord length on the pressure side to 35% chord length on the suction side (*LE-2*). This recess allows a DBD plasma actuator to be flush-mounted near the leading edge to avoid significant discontinuities on the surface. The two *LE* pieces are necessary for characterization since placement of an actuator on the model does not permit complete  $C_p$ , and subsequent  $C_L$ , measurement due to obstruction of pressure taps near the *LE*. Experiments are performed at angles of attack up to  $20^\circ$ , which corresponds to approximately 12% blockage. No blockage or wall-corrections have been used.

## 2.2. Flow Diagnostics

The airfoil is equipped with static pressure taps distributed around the chord near the center of the span as shown in Figure 2. Static pressure measurements are acquired using Scanivalve digital pressure sensor arrays (DSA-3217). In post-processing, values of sectional  $C_p$  and  $C_L$  are averaged over 50 samples acquired at 5 Hz. Six dynamic pressure transducers mounted flush with the surface of the suction side of the airfoil are capable of acquiring high-bandwidth data, but are not employed in this work. An array of Senflex<sup>®</sup> hot film sensors is adhered to the suction side of the airfoil from 37% to 63% chord length and on the pressure side from 11% to 17% chord length (Figure 2 and Figure 3). These devices respond to changes in the shear stress on the surface of the airfoil. Only the pressure side sensor at  $x/c = 11\%$  is employed here. A four-channel constant-voltage anemometer (Tao Systems, Inc.) provides the necessary excitation. The pressure side sensor at  $x/c = 11\%$  is used to track movement of the stagnation line during closed-loop control. Shifts in the stagnation line result in a change in the power dissipated by the hot film sensor near the leading edge. This shift in the stagnation line can be

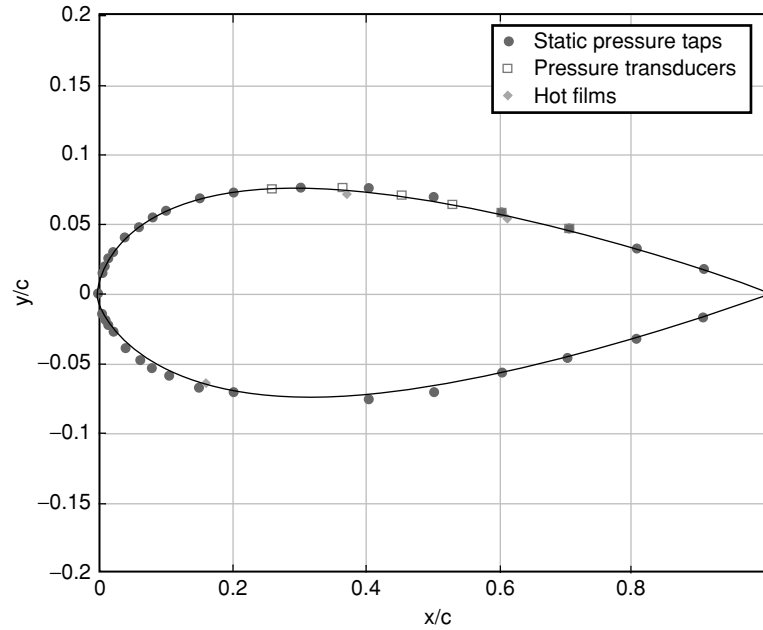


Figure 2. Locations of sensors on the NACA 0015 airfoil (not to scale).

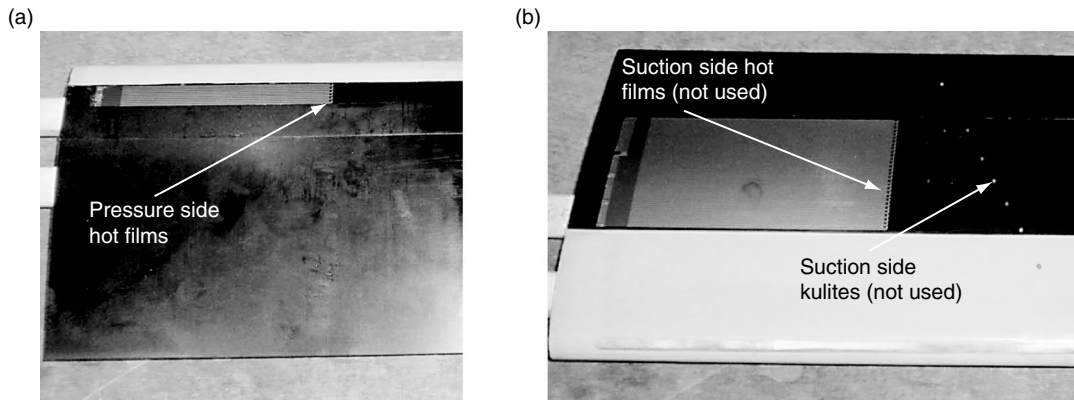


Figure 3. NACA 0015 airfoil with leading edge actuator installed (LE-2): view of (a) pressure side, and (b) suction side.

correlated to changes in the static pressure distribution, and consequently is a surrogate for  $C_L$  (Poggie *et al.* 2010). The power dissipated ( $P_{HF}$ ) by the hot film sensors is calculated using the resistance of the sensor and the applied constant voltage across the sensor. The resistance ( $R_{HF}$ ) is calculated using the excitation voltage ( $V_w = 1.18$  V) and the measured sensor output voltage ( $V_s$ ), which is low-pass filtered at 8 kHz, along with constants  $a = 0.0085$  and  $b = -0.0097$  which are specific to the data acquisition and signal conditioning hardware. The relevant expression as specified by Tao Systems, Inc. is:

$$P_{HF} = \frac{V_w^2}{R_{HF}} \quad (1)$$

$$R_{HF} = \frac{1}{a \left( \frac{V_s}{V_w} \right) + b} \quad (2)$$

Two-component particle image velocimetry (PIV) is used to obtain quantitative measurements of the velocity field over the airfoil. Images are acquired and processed using a LaVision PIV system. Nominally submicron olive oil seed particles are introduced upstream of the test section contraction using a 6-jet atomizer. A dual-head Spectra Physics PIV-400 Nd:YAG laser is used in conjunction with spherical and cylindrical lenses to form a thin light sheet that allows PIV measurements. The time separation between laser pulses used for particle scattering is set according to the flow velocity, camera magnification and correlation window size. Two images corresponding to the pulses from each laser head are acquired by a LaVision 14 bit 2048 by 2048 pixel Imager Pro-X CCD camera equipped with a Nikon Nikkor 50 mm  $f/1.2$  lens. For each image pair, subregions are cross-correlated using decreasing window size ( $64^2$ – $32^2$  pixels) multi-pass processing with 50% overlap. The resulting velocity fields are postprocessed to remove spurious vectors using an allowable vector range and median filter. Removed vectors are replaced using an interpolation scheme based on the average of neighboring vectors. A  $3 \times 3$  Gaussian smoothing filter is also applied to the calculated velocity fields.

Phase-locked PIV data are acquired using the programmable timing unit of the LaVision system. The acquisition is synced with the frequency of the actuation signal. Velocity fields at various phases of the actuator modulation frequency are investigated by stepping through the actuation period using time delays. The resulting phase-locked data sets are averaged over 125 images at each phase which is sufficient for resolving the primary features of the flow fields (i.e. coherent structures). Eight phases of the NS-DBD actuator controlled flow fields are acquired, but only four phases are presented here in the interest of brevity. Phase-locked PIV data are acquired at 5 Hz. The spatial resolution of PIV data for the airfoil is approximately 2.2 mm.

The full-scale accuracy for all instantaneous velocity fields is less than 1% assuming negligible laser timing errors and a correlation peak estimation error of 0.1 pixels. The 95% confidence interval for  $C_p$  and hot film measurements is smaller than the presented symbol size. The repeatability of the results is primarily determined by the manual setting of incidence angles ( $\pm 1/4^\circ$ ) and the accuracy with which the actuator can be constructed and adhered to the surface ( $\pm 0.5\%$  of chord).

### 2.3. DBD Plasma Actuators

The DBD plasma actuators used in these experiments consist of asymmetric electrodes separated by a dielectric layer as shown in Figure 4. Two different types of actuators have been used. All open-loop and extremum-seeking feedback control work presented here is performed using Kapton tape-based actuators. These actuators have electrodes made of copper tape with a dielectric consisting of layers of Kapton tape. The covered ground electrode is 12.7 mm (1/2 inch) wide and the exposed high voltage electrode is 6.35 mm (1/4 in) wide. Both electrodes have thickness of 0.09 mm (3.5 mil). The dielectric barrier is composed of 3 layers of Kapton tape. Each layer has thickness of 0.09 mm (3.5 mil) and dielectric strength of 10 kV. Each layer of Kapton tape has a 0.04 mm (1.5 mil) layer of silicone adhesive such that the actual Kapton thickness for each tape layer is only 0.05 mm (2 mil). The total thicknesses of the dielectric and the device as a whole are 0.27 mm (10.5 mil) and 0.44 mm (17.5 mil), respectively. The dielectric is wrapped around the  $LE-2$  recess to remove discontinuities.

A printed circuit board (PCB) actuator is used with the on/off controller. Open-loop experiments have also been performed with this type of actuator, and results are similar to those obtained with Kapton tape actuator. The PCB actuator is made of a 0.127 mm (5 mil) thick polyimide dielectric clad in 0.025 mm (1 mil) copper laminate on both sides (Dupont Part FR8555R). This copper layer is etched away from the dielectric to produce the necessary electrode geometry (Figure 3 and Figure 4). The PCB actuators are preferred for their improved fabrication repeatability. For both types of

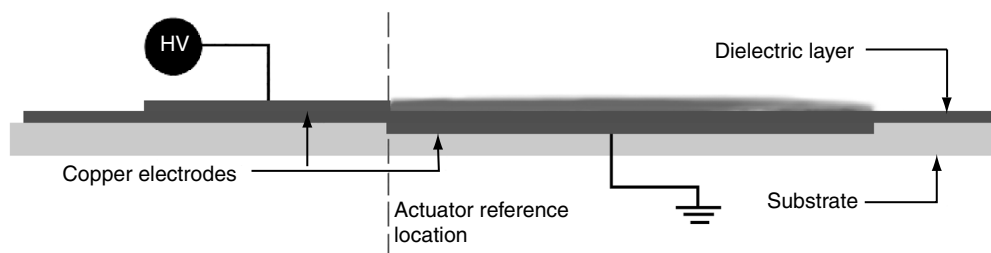


Figure 4. DBD plasma actuator schematic.

actuators, the substrate consists of layers of Kapton tape necessary to fill the leading edge recess. These passive dielectric layers are necessary to make the top of the actuator flush with the airfoil surface when installed. The recess is intentionally designed in this fashion so thicker dielectrics could be employed in the future. The interface for both types of actuators is set at  $x/c = 1\% \pm 0.5\%$  with upstream orientation for NS-DBD and downstream orientation for AC-DBD experiments (see Figures 3 and 4).

The repetitive nanosecond pulse voltage waveform for the surface DBD discharge is generated by high-voltage magnetic compression type pulsed power supplies, custom designed and built at The Ohio State University. Briefly, these power supplies generate high voltage pulses (peak voltage up to 20 kV, pulse duration 50–100 nsec FWHM), at a continuous pulse repetition rate of up to 3 kHz, and pulse energy of up to 100 mJ/pulse. There is no lower bound on the repetition rate and no low frequency burst or amplitude modulation is performed in this work. Both the peak voltage and the pulse energy are strongly load-dependent. The pulse waveform is transmitted to the DBD actuator load via a collinear pair of transmission lines up to 1.5 m long. The pulser creates short duration pulses of approximately 100 ns FWHM for the current conditions. A sample waveform is shown in Figure 5. Peak voltage is  $\sim 8.5$  kV and the pulse energy is on the order of 0.5 mJ/cm. Figure 6 shows a phase-averaged schlieren image

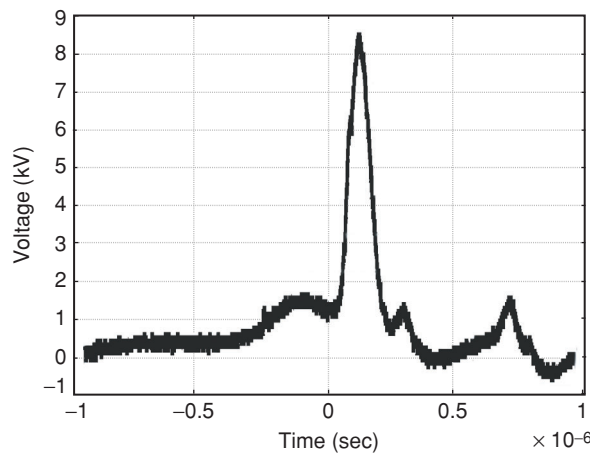


Figure 5. Sample high voltage pulse.

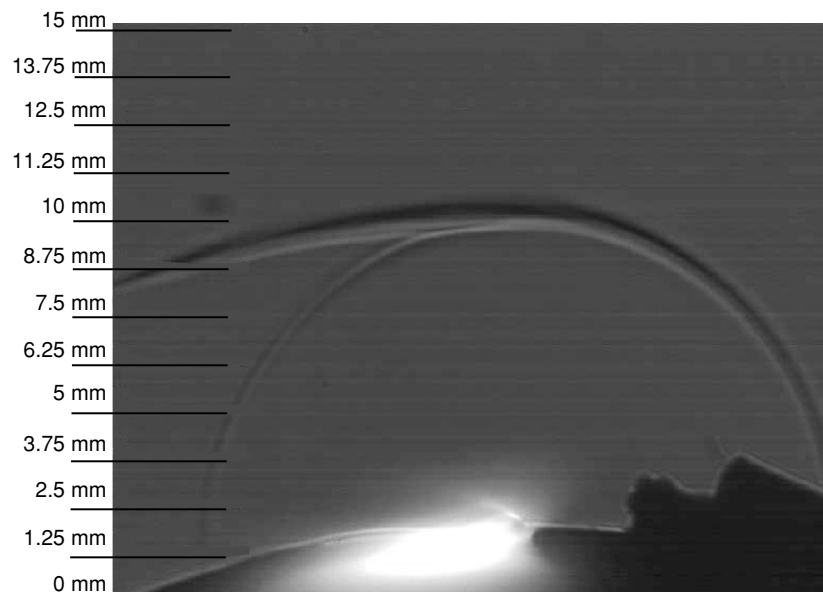


Figure 6. Phase-averaged schlieren image of a compression wave generated by NS-DBD plasma actuator viewed along the major axis of the actuator.

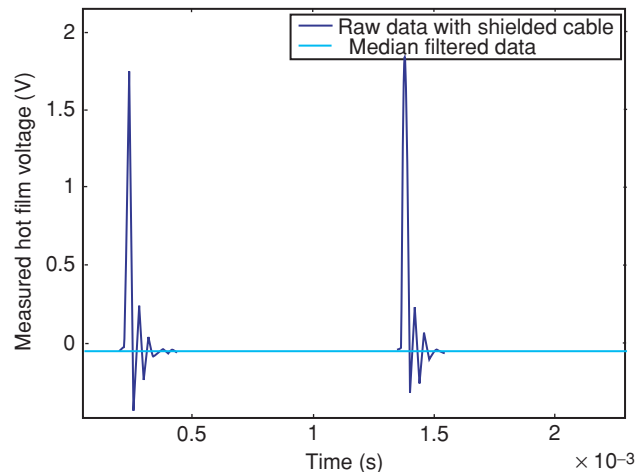


Figure 7. Hot film median filter signal processing example.

of a compression wave that is created by the NS-DBD actuator operated in quiescent air. This compression wave is generated by the thermal effects of the plasma (Joule heating). Unlike AC-DBDs, the thermal effect is believed to be the main control mechanism for NS-DBD plasma actuation. The details of the plasma hardware and the physics of actuation have been discussed in our previous work (Little *et al.* 2012; Takashima *et al.* 2011). The shape of each pulse is determined by the internal hardware of the power supply, but the timing of the pulses is dictated by a rapid prototyped controller running on a dSpace DSP 1103 board. The dSpace hardware and software are also used for rapid prototyping and evaluation of the closed-loop control strategy.

Like all plasma actuators, the electromagnetic interference (EMI) of the NS-DBD can be problematic. An example of NS-DBD EMI in the hot film signal is shown in Figure 7. NS-DBD EMI is manifested as unphysical impulse-like spike in time trace, which effectively represents the high voltage pulse. In this work, we are only concerned with the mean value of the hot film signal. This and the unphysical nature of the EMI disturbance permit removal using a 12-point median filter in the time domain. An example of the filtered and unfiltered signal is provided in Figure 7. This is implemented within the signal processing block of the feedback controller. It should be noted that all cabling and connections are carefully shielded and multiple ferrites are employed before using these signal processing techniques. We have not encountered issues with EMI for any of the other instrumentation employed in this work.

Input signals for the AC-DBD plasma are generated using the same dSpace hardware and software used for the NS-DBD plasma. The input signal is sent to a Powertron Model 1500S AC power supply and step-up transformer. The amplified signal is then sent to a low power (200W), high voltage (0–20 kV<sub>rms</sub>) transformer designed to operate in a frequency range of 1–5 kHz. Voltage measurements are acquired and monitored at the secondary side of the high voltage transformer with a Tektronix P6015A probe. The AC signal uses a 2 kHz carrier frequency,  $f_c$ , to produce the plasma. This signal is modulated at a lower frequency,  $f_m$ , to excite natural flow instabilities in certain flow regimes. The maximum velocity generated by the AC-DBD actuator in quiescent air measured 20 mm downstream of the electrode interface is between 3 and 3.5 m/s for a 2 kHz carrier frequency with no modulation. The velocity profile is affected by changes in supply voltage, carrier frequency, and any modulation of the signal. In contrast, 2 kHz operation of the NS-DBD produces only  $\sim 0.5$  m/s (Little *et al.* 2012). The power consumption of both types of DBD actuators used in this work is similar ( $\sim 1$  W/cm). However, the NS-DBD actuator requires a significantly larger peak power during the nanosecond pulse. It is important to note that neither of these actuators has been fully optimized for aerodynamic performance or power.

### 3 RESULTS

#### 3.1. Baseline Results

Baseline NACA 0015 characteristics are determined using the leading edge with no recess (*LE-1*).  $C_L$  is calculated by integrating  $C_p$  values on the surface of the airfoil. The Prandtl-Glauert transformation is used to adjust for compressibility effects although they are very small. The maximum lift coefficient,  $C_{L,max}$ , is found around  $12^\circ$  for all  $Re$ , although the value of  $C_{L,max}$  is dependent on  $Re$

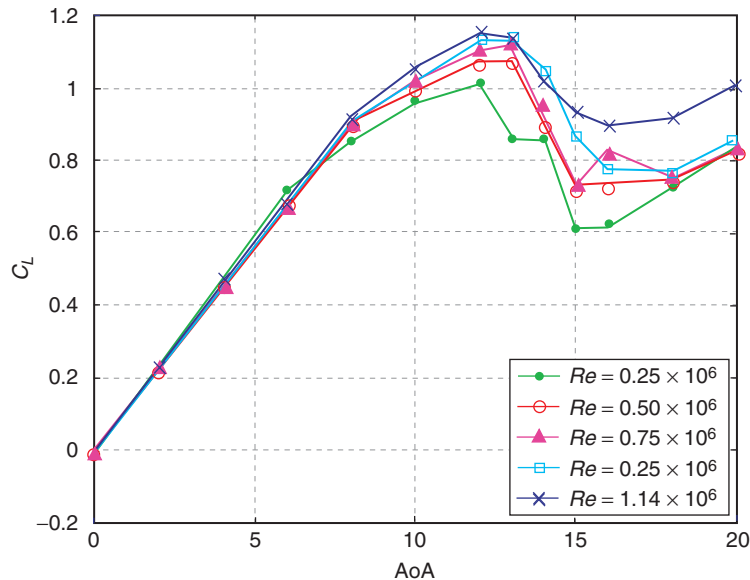


Figure 8. Lift coefficient vs. angle of attack for various Reynolds numbers for the baseline case.

as expected (Figure 8). This is most apparent when considering the change in performance between  $Re = 0.25 \times 10^6$  and  $1.15 \times 10^6$  at  $\alpha = 12\text{--}13^\circ$ , where the low- $Re$  behavior is likely caused by laminar boundary layer separation. The range of  $C_{L,max}$  between all  $Re$  considered is 1.0–1.2. The post-stall form of the lift curve is strongly dependent on  $Re$  due to slight variations in  $LE$  boundary layer separation location. The different behaviors shown in Figure 8 necessitate different control strategies depending on  $Re$  and  $\alpha$ . For example, at  $Re = 0.25 \times 10^6$  and  $\alpha = 12\text{--}14^\circ$  an active boundary layer trip should be sufficient to increase  $C_L$  to values observed in the high  $Re$  baseline case. However, at high  $Re$  ( $1.15 \times 10^6$ ) and post-stall ( $\alpha = 18^\circ$ ) transition alone is unlikely to reduce separation. We provide evidence of these two mechanisms in the following discussion.

A comparison between  $LE-1$  and  $LE-2$  without control is shown in Figure 9. This is done by installing an actuator on  $LE-2$  with no plasma formation. This represents the passive effect of the DBD actuator on the airfoil  $C_p$  distribution. Four angles of attack and two actuators types are shown in Figure 9. No data is acquired at the  $LE$  in close proximity to the electrodes, but further downstream starting at  $x/c = 6\%$ , holes are made in the dielectric to allow static pressure measurements using the underlying taps. The location for these holes is chosen such that it is far enough downstream to prevent arc formation. The change in  $LE$  surface condition has some effect on the baseline pressure distribution for incidence angles near  $C_{L,max}$  (Figure 9a and 9c). It should be noted, that physically identical actuators can result in leading edge pressure distributions anywhere in the range encompassed by Figures 9a and 9c. This is not surprising given the sensitivity of the boundary layer to the leading edge surface conditions especially near the stall angle. Such results are also influenced by manual settings of angle of attack which have uncertainty of approximately  $\pm 1/4^\circ$ . These repeatability issues are not encountered at post-stall conditions as shown in Figures 9b and 9d. The pressure distributions are nearly identical in these cases which are the focus of this work. This confirms that the actuator is not functioning as a passive control device and any control authority obtained is due to plasma formation in the results that follow.

A baseline characterization of the hot film response to changing flow conditions is also performed. The signal from the hot film sensor nearest the  $LE$  ( $x/c = 11\%$ ) is used as the input to the closed-loop controllers shown later. This sensor is as close to the leading edge as one can possibly instrument for the chosen airfoil construction and actuator geometry. It is used to obtain a relative estimate of the stagnation line location near the leading edge of the airfoil, which is related to  $C_L$ . When an actuator is present, the complete  $C_p$  distribution cannot be obtained due to installation of the actuator at the  $LE$ . Consequently, accurate  $C_L$  computations are not possible because the greatest contribution to the change in lift is expected to be due to static pressure changes at the leading edge caused by the control.

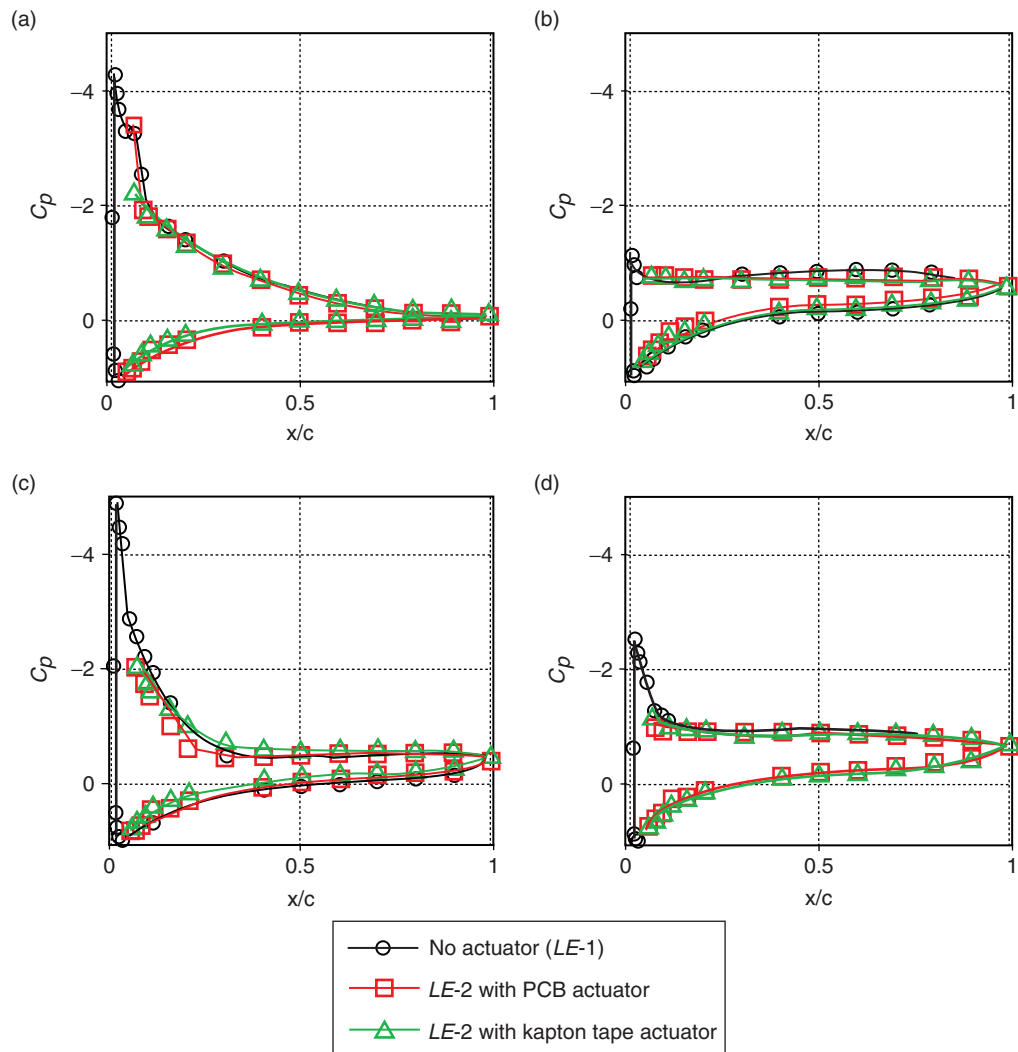


Figure 9. Baseline  $C_p$  comparison for clean airfoil ( $LE-1$ ) and airfoil with recess and actuator ( $LE-2$ ) (a)  $Re = 0.25 \times 10^6$ ,  $\alpha = 12^\circ$ , (b)  $Re = 0.25 \times 10^6$ ,  $\alpha = 14^\circ$ , (c)  $Re = 1.15 \times 10^6$ ,  $\alpha = 14^\circ$  and (d)  $Re = 1.15 \times 10^6$ ,  $\alpha = 16^\circ$ .

Therefore, the  $C_p$  value measured closest to the leading edge on the suction side ( $C_{p-LE}$  measured at  $x/c = 6\%$ ) will be used as an indicator of the change in  $C_L$ . The correlation between this simplified estimate is validated by comparing the  $C_{p-LE}$  values in Figure 10 with the  $C_L$  curves in Figure 8. A more negative value of  $C_p$  close to the leading edge should generally correspond to a higher lift. Both the  $C_{L,max}$  value that occurs at  $\alpha = 12^\circ$  and  $C_L$  decrease at  $\alpha = 14^\circ$  are indicated by the  $C_{p-LE}$  values in Figure 10. The hot-film signal is less sensitive to the changing conditions especially in the high  $Re$  case (Figure 10b) at post-stall ( $\alpha > 12^\circ$ ). Implications and a potential explanation for this are addressed in the following discussion.

To assist in explanation of the hot film signal, we employ the analysis tool XFLR5, a successor to the popular code XFOIL. Figure 11 presents XFLR5 predictions of pressure side  $C_f$  near the leading edge of a NACA 0015 at  $Re = 1 \times 10^6$  for two sample angle of attacks. Predictions for the suction surface have been removed for simplicity. Note the large difference in  $C_f$  gradient on two sides of the stagnation line. Upstream of stagnation the  $C_f$  gradient is substantial while downstream the gradient is quite small. As  $\alpha$  and  $C_L$  increase, the stagnation line moves downstream on the pressure side of the airfoil. At post-stall  $\alpha$ , the stagnation line moves back upstream corresponding to a decrease in  $C_L$ . These changes result in shifts of the shear stress profile allowing the hot film to track movement of the stagnation line. The performance of feedback control crucially depends on the quality of the measured

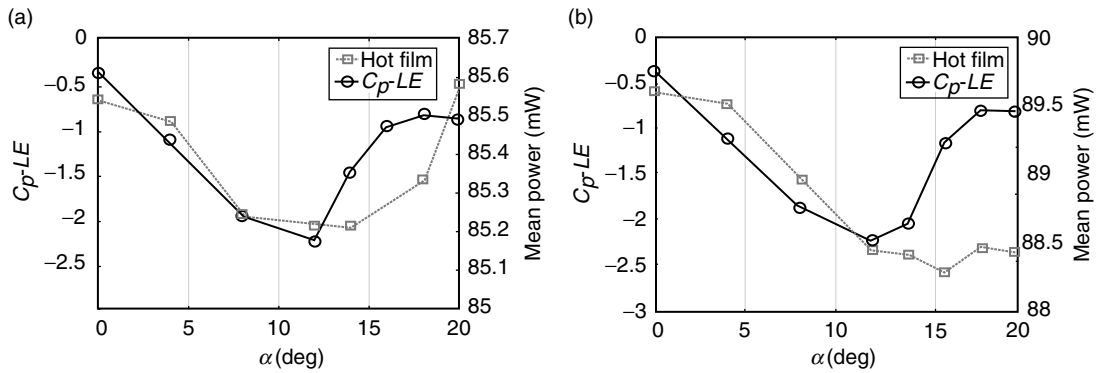


Figure 10. Baseline  $C_p$ -LE and hot film power dissipated vs.  $\alpha$  for (a)  $Re = 0.25 \times 10^6$  and (b)  $Re = 1.15 \times 10^6$  for LE-2.

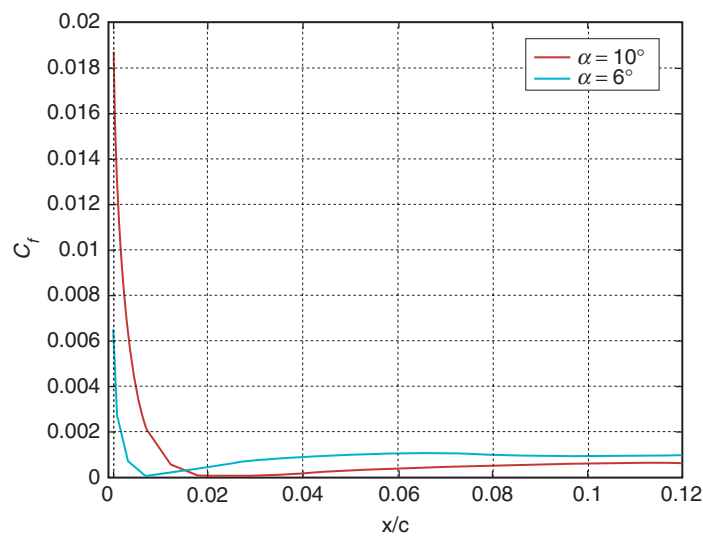


Figure 11. XFLR5 predictions of pressure side skin friction near the leading edge of a NACA 0015 at  $\alpha = 6^\circ$  and  $10^\circ$  for  $Re = 1.00 \times 10^6$ .

signal employed as a surrogate for the performance objective. The curves of Figure 11 illustrate that for increased sensitivity, a hot film sensor should be located upstream of stagnation in the region of high  $C_f$  gradient such that small movements of the stagnation line can be resolved. Unfortunately, the actuator recess employed in this work requires sensors placed further downstream at  $x/c = 11\%$  to prevent damage due to actuator placement. This design was chosen to safely ensure substantial distance between the plasma discharge and the hot film sensor and could be reduced in future studies. The data in Figure 11 qualitatively explain the poor sensitivity observed in Figure 10. Based on this information, it is somewhat surprising that movement of the stagnation line can be tracked at all this far downstream yet useful results have been obtained. Increased sensitivity is expected if sensors could be placed upstream of the stagnation line in the region of strong shear stress gradient. For example, in Poggie *et al.* (2010) a hot film sensor at  $x/c = 0.17\%$  showed increasing shear stress with increasing  $C_L$  indicating it is on the upstream of stagnation. In our case ( $x/c = 11\%$ ), shear stress decreases with increasing  $C_L$ , consistent with data of Figure 11. Thus, both the sensitivity and sign of the  $C_L$ - $C_f$  correlation are dependent on the sensor location relative to the stagnation line.

### 3.2. NS-DBD Open-Loop Control

Open-loop control characterization of both the actuators as well as the response of the hot film sensors is performed at various  $Re$  and post stall  $\alpha$ . A comparison between the effects of actuation with the PCB

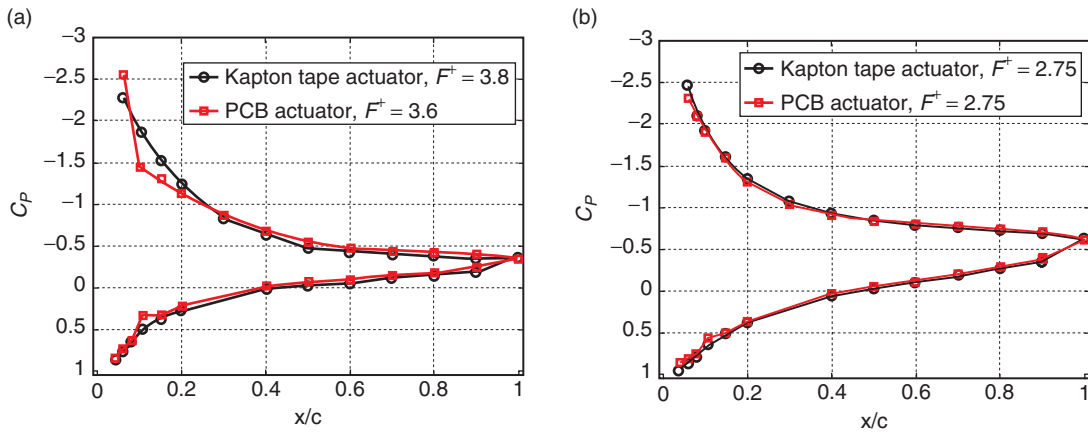


Figure 12.  $C_p$  comparison for airfoil with Kapton tape actuator and for airfoil with PCB actuator: (a)  $Re = 0.25 \times 10^6$ ,  $\alpha = 14^\circ$  and (b)  $Re = 1.15 \times 10^6$ ,  $\alpha = 20^\circ$ .

actuator and the Kapton tape actuator is shown in Figure 12. This is performed in order to ensure that control authority is reasonably similar. In the low  $Re$  case (Figure 12a) there is some discrepancy in performance especially near the leading edge. Small differences like this are seen even with the same type of actuator due to the sensitivity of the leading edge boundary layer to actuator imposed surface discontinuities and/or slight variations in angle of attack near stall. Similar behavior is also seen in the baseline case (Figure 10a). Despite the differences in performance it is clear that both types of actuators create beneficial effects. At higher  $Re$  and  $\alpha$  (Figure 12b), control authority is nearly equivalent between the two constructions. This is consistent throughout the work and can be explained by considering that the electrodes are now further downstream from the stagnation line thus encountering a thicker and likely turbulent boundary layer in these conditions. It should be noted that the focus of the paper is not on direct comparison of the two actuators. Instead, we wish to provide results that validate the use of similar control strategies for both types of actuator.

There are several well-established mechanisms for separation mitigation in airfoils. Examples include tripping the boundary layer at low  $Re$ , exciting natural instabilities in the flow, and adding momentum or removing the boundary layer via steady blowing/suction (Greenblatt and Wygnanski 2000). Recent work has shown that NS-DBD actuators do not possess significant EHD effects (Roupassov *et al.* 2009; Little *et al.* 2012) thus any effect due to blowing can be ruled out at the freestream velocities considered here. The remaining control mechanisms (boundary layer tripping and instability excitation) have been observed depending on  $Re$  and  $\alpha$ . Open-loop control results for these mechanisms at two representative flow conditions are shown in Figures 13 and 14. Figure 13 presents a low  $Re$  ( $0.25 \times 10^6$ ) moderate  $\alpha$  ( $14^\circ$ ) case.  $Re$  has a considerable effect on  $C_L$  at this  $\alpha$  as seen in

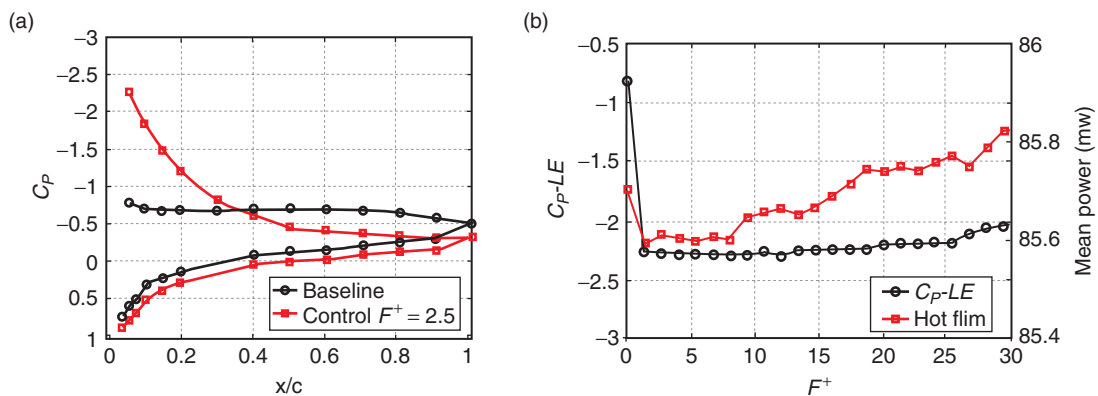


Figure 13. (a)  $C_p$  curves for baseline and with control using NS-DBD at  $F^+$  of 2.5 and (b) hot film dissipated power and  $C_{p-LE}$  for various forcing frequencies, for  $Re = 0.25 \times 10^6$ ,  $\alpha = 14^\circ$ .

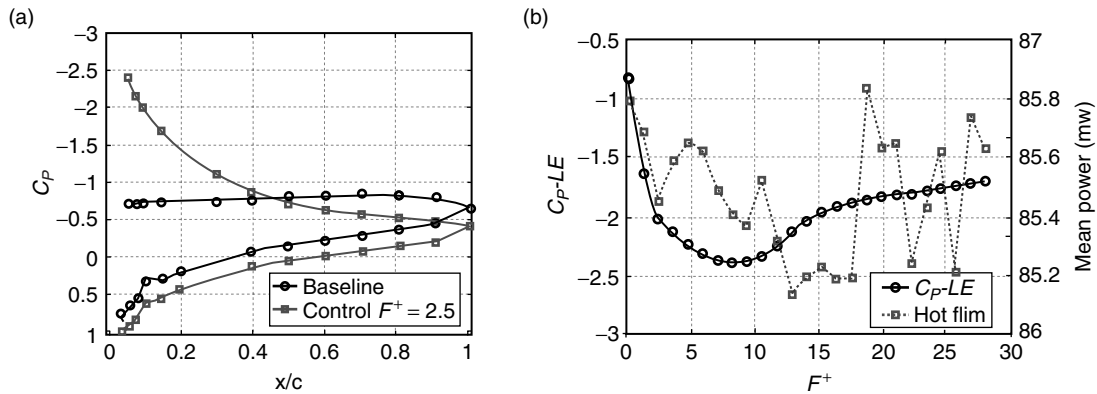


Figure 14. (a)  $C_p$  curves for baseline and with control with NS-DBD at  $F^+$  of 1.9 and (b) hot film dissipated power and  $C_{p-LE}$  for various forcing frequencies, for  $Re = 1.15 \times 10^6$ ,  $\alpha = 18^\circ$ .

Figure 8, suggesting boundary layer transition effects are important here. Sample  $C_p$  distributions as well as the response of both  $C_{p-LE}$  and the hot film sensor located at  $x/c = 11\%$  on the pressure side are provided. Figure 13(a) shows the baseline  $C_p$  distribution which is characterized by a near-zero pressure gradient on the suction side. Actuation of NS-DBD at  $F^+ = 2.5$  attaches flow to most of the suction surface. In the present work, the hot film sensors are placed substantially aft of the stagnation line on the pressure side; yet a measureable relation with suction side  $C_{p-LE}$  can still be observed (Figure 13(b)). The  $C_p$  data in Figure 13(a) shows that the stagnation line is at  $x/c < 5\%$ ; thus it is somewhat surprising that its motion is tracked at all so far downstream, especially with this low velocity flow (see Figure 11). Examination of Figure 13(b) shows a positive relationship between suction side  $C_{p-LE}$  and pressure side hot film near the  $LE$ . Note that baseline values are shown at  $F^+ = 0$ . It is also important to recognize that the change in the hot film signal ( $< 0.2$  mW) is quite small compared to the nominal value ( $\sim 85$  mW). The response of  $C_p$  to forcing frequency is constant from  $F^+ = 2$ –12, and no preferred frequency can be distinguished. At higher frequency, the  $C_{p-LE}$  value increases slightly indicating reduced control authority. The hot film signal captures this behavior up to  $F^+ = 8$ , but higher frequency excitation causes the mean power to increase above the baseline value in contrast to the  $C_p$  data. These flow conditions (low  $Re$ , moderate  $\alpha$ ) correspond to a case where a well-designed  $LE$  boundary layer trip can reattach the flow to the suction surface. This, along with the lack of a preferred frequency in Figure 13(b), suggests that the actuator functions as an active trip. This behavior has previously been observed for a different airfoil (Little *et al.* 2012).

Figure 14 considers the case of both high  $Re$  ( $1.15 \times 10^6$ ) and post-stall  $\alpha$  ( $18^\circ$ ). The baseline is characterized by deep stall and actuation with NS-DBD at  $F^+ = 1.9$  reattaches flow to most of the suction surface (Figure 14(a)). The frequency sweep result shown in Figure 14(b) is quite different from that previously examined for low  $Re$  (Figure 13(b)). A clear preference is seen for  $F^+ = 1.9$ , which is generally consistent with dimensionless frequencies observed in literature ( $F^+ \approx 1$ ) (Seifert *et al.* 1996). This indicates a different control mechanism from the one in Figure 13. Correlation between suction side  $C_{p-LE}$  and the hot film signal is substantially less apparent for these conditions. While the minimum for  $C_p$  occurs at  $F^+ = 1.9$ , the corresponding minimum for the hot film signal is near  $F^+ = 3$ –4. Moreover, there is substantial scatter in the hot film data. It is unclear if this is a result of the control mechanism, which is fundamentally different from that observed in Figure 13, or a characteristic of the hot film reaction to changes in the shear stress distribution at such high angle of attack. Further studies are required to explain these results.

The frequency sweep results presented in Figure 13 and 14 show that two different control mechanisms are at play. In the low  $Re$ , low- $\alpha$  case, the frequency of actuation is not critical. This behavior indicates that flow instabilities are not being excited and the actuator is acting as an active boundary layer trip as previously observed on the NASA EET airfoil (Little *et al.*, 2012). The excitation of natural flow instabilities is largely dependent on the frequency of excitation. This is shown in Figure 14 where a clear frequency preference of around  $F^+ = 1.9$  is seen. This indicates that the primary method of control in these high  $Re$ , high- $\alpha$  conditions is the generation of large scale structures through the excitation of shear layer instabilities. The presence of coherent structures in the flow is confirmed by PIV results shown in

Figure 15. Coherent spanwise vortices are identified using swirling strength. Unlike out-of-plane vorticity which identifies both rotation and shear, this technique ignores regions of pure shear and highlights regions of pure rotation. The method is based on critical point analysis of the local velocity gradient tensor and its eigenvalues (Adrian *et al.*, 2000). In two-dimensional form, the velocity gradient tensor is:

$$\nabla \tilde{W} = \begin{pmatrix} \frac{\partial \tilde{U}}{\partial x} & \frac{\partial \tilde{U}}{\partial y} \\ \frac{\partial \tilde{V}}{\partial x} & \frac{\partial \tilde{V}}{\partial y} \end{pmatrix} \quad (3)$$

where in this case the gradient has been applied to the phase-averaged velocity field,  $\tilde{W}$ . The parameter of interest is the imaginary component of the eigenvalues of Equation 3, which is nonzero only if:

$$\frac{\partial \tilde{U}}{\partial y} \frac{\partial \tilde{V}}{\partial x} - \frac{1}{2} \frac{\partial \tilde{U}}{\partial x} \frac{\partial \tilde{V}}{\partial y} + \frac{1}{4} \left[ \left( \frac{\partial \tilde{U}}{\partial x} \right)^2 + \left( \frac{\partial \tilde{V}}{\partial y} \right)^2 \right] < 0 \quad (4)$$

The gradient tensor in Equation 3 is computed using a 2<sup>nd</sup> order accurate central difference scheme. The magnitude of the imaginary component of its eigenvalues,  $\lambda_{ci}$ , is normalized as  $\lambda_{ci}^* = \lambda_{ci} c / U_\infty$  and the results are shown in Figure 15.

Coherent structures dominate the flow field and the number of these structures is consistent with forcing at  $F^+ = 2.75$ . Four phases ( $\Delta\Phi = \pi/2$ ) of the actuation period clearly demonstrate the propagation of these organized regions along the airfoil chord. As expected, the coherent motion begins to break up further downstream ( $x/c > 0.6$ ). These vortices entrain and transfer high momentum fluid into the separated region near the airfoil surface. The dynamic content suggests that the control mechanism at high  $\alpha$  is not laminar to turbulent transition, but rather the excitation of flow instability through NS-DBD generated thermal perturbations. The data in Figure 15 are shown to illustrate this effect which is present for all high  $\alpha$  conditions ( $>16^\circ$ ) examined in this work.

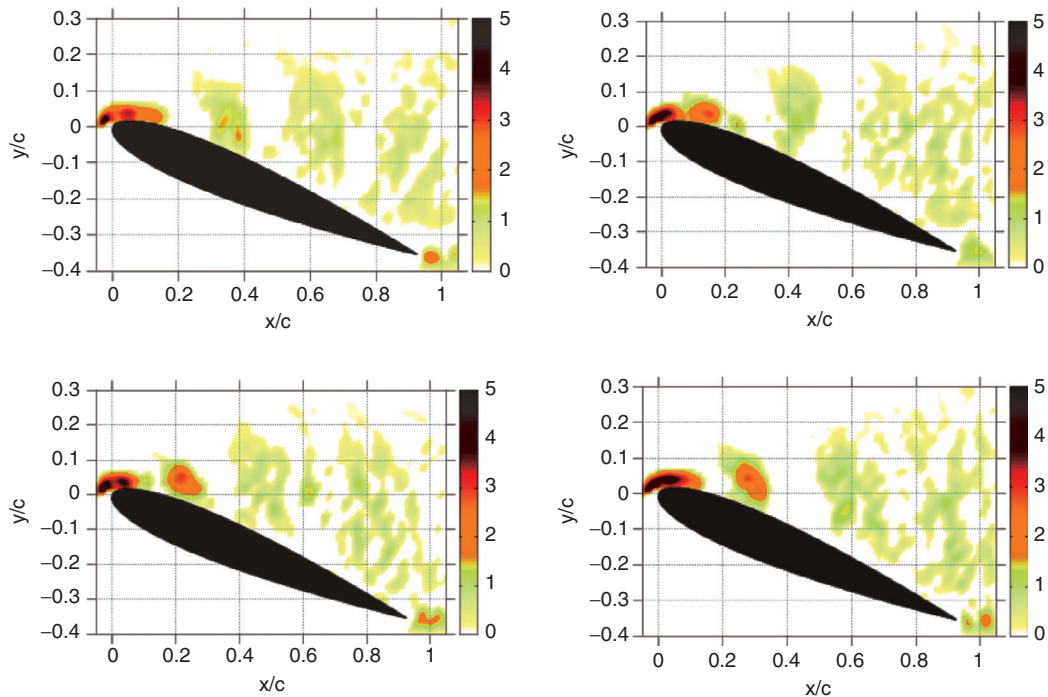


Figure 15. Four ( $\Delta\Phi = \pi/2$ ) phase-averaged normalized swirling strength images,  $\lambda_{ci}^*$ , for NS-DBD plasma actuator forcing at  $F_c^+ = 2.75$  at  $Re = 1.15 \times 10^6$ ,  $\alpha = 20^\circ$ .

This mechanism is widely established in the literature for controlling separation in many flow systems (Greenblatt and Wygnanski 2000). However, this behavior has not been consistently demonstrated at these conditions for more common AC-DBD plasma actuators that function through a fundamentally different mechanism (EHD force). Spanwise vortices have been visualized over a range of actuation frequencies on a different airfoil (Little *et al.* 2012). It is believed that the control mechanism stems from rapid localized heating of the near-surface flow by the plasma. This produces local compression waves similar to LAFPA that have shown control authority for various high  $Re$  and high  $M$  jets (Samimy *et al.* 2010). Figure 15 is an important result which shows the efficacy of NS-DBD plasma for generating coherent structures and controlling flow separation at  $Re = 1.15 \times 10^6$  and  $M = 0.26$  ( $U_\infty = 93$  m/s) which are realistic aircraft takeoff and landing conditions. It is also in agreement with the results of Roupassov *et al.* (2009), which used a shorter pulse width NS-DBD waveform with similar success.

### 3.3. Comparison of NS-DBD and AC-DBD Open-Loop Control

A brief comparison of AC-DBD and NS-DBD plasma actuators is provided to investigate differences in their control authority. In the AC-DBD plasma actuator experiments the actuator has an equivalent construction to the NS-DBD actuator, with the only difference being that copper electrodes are mirrored about the actuator interface so that the plasma forms on the downstream side of the exposed electrode. This is the standard AC-DBD configuration and in this configuration the induced body force is in the downstream direction. It should be noted that for the AC-DBD plasma tests the  $C_p$  value could not be measured as close to the leading edge as compared to the NS-DBD plasma due to the differences in actuator orientation and plasma extent.

The AC-DBD experiments are performed at  $\alpha = 18^\circ$  while varying  $Re$ . The AC signal is approximately 18 kVpp for all testing. The carrier frequency of the AC-DBD actuator is 2 kHz and the signal is duty-cycle modulated at different frequencies with the best case for each flow regime shown in Figure 16. The response to changes in frequency of actuation for both AC- and NS-DBD plasma actuators was found to be very similar. Varying the duty cycle was found to have very little effect on control authority, and the data presented is for a 20% duty cycle.

A comparison of the  $C_p$  curves in Figure 16(a) shows that the effectiveness of the AC-DBD actuator drops off significantly as  $Re$  is increased, with almost no discernible control authority beyond  $Re = 0.50 \times 10^6$  (39 m/s) which is consistent with results in literature (Moreau 2007). The AC-DBD actuator creates a strong suction peak near the leading edge of the airfoil similar to the NS-DBD actuator at  $Re = 0.25 \times 10^6$ . However, at  $Re = 0.50 \times 10^6$  the  $C_p$  curve shows a much smaller change with AC-DBD plasma actuation, indicating a reduction in effectiveness of the device. At  $Re = 0.75 \times 10^6$  and above the AC-DBD actuator exhibits almost no control authority on the separated flow. The reason for this reduction in control authority at higher flow velocities is that the control mechanism of the AC-DBD actuator is an EHD effect that creates a pulsed wall jet on the airfoil surface. This pulsed wall jet adds momentum to the flow near the wall to help the boundary layer to overcome the adverse pressure gradient to mitigate separation. But as the flow velocity is increased the relative effect of adding the same momentum is reduced, thereby limiting the velocity at which AC-DBD plasma actuation is effective for flow control. The NS-DBD plasma actuator,

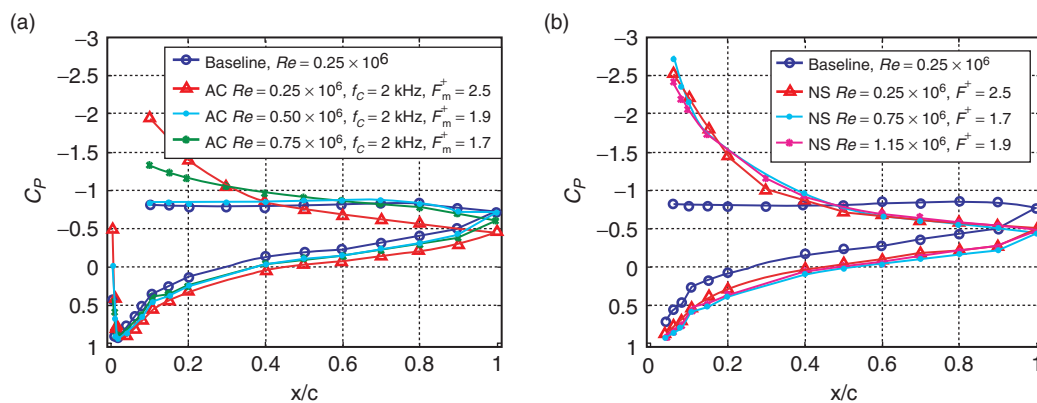


Figure 16.  $C_p$  curves at  $\alpha = 18^\circ$  and varying  $Re$  for (a) AC-DBD and (b) NS-DBD actuation.

by comparison shows similar control authority to that seen at  $Re = 0.25 \times 10^6$  with the AC-DBD actuator up to the maximum speed of the wind tunnel ( $Re = 1.15 \times 10^6$ ). These results are in agreement with our previous experiments on a different airfoil (Little *et al.* 2010).

### 3.4. Closed-Loop Control

Closed-loop control is investigated over a range of  $Re$  and  $\alpha$  using the hot film sensor nearest stagnation ( $x/c = 11\%$ ) as a control input. An on/off controller is designed to operate based on the mean value of the power dissipated by the hot-film which changes based on the movement of the stagnation line (see Figures 11, 13–14). The change in hot film signal is small due to sensor location which is aft of stagnation line on the pressure side of the airfoil. This small change results in a low signal to noise ratio for the ‘control input’ of the closed-loop controller, and taking a mean value over a short time period increases this signal to noise ratio. Attempts to calibrate the sensor response in open-loop control experiments have met with limited success (Figures 13b and 14b). However, the theoretical  $C_F$  distribution suggests that minimization of the hot film output should provide the highest  $C_L$  (see Figure 10–11). Figure 17 depicts the on/off controller schematic. A nominal threshold and a dead zone width are set based on experience gained in previous open-loop experiments. These settings are such that a reading of dissipated power above the dead zone indicates separated flow, whereas one below it indicates attached flow (see Figures 11, 13b and 14b). A dead zone is used rather than a single threshold value to avoid unsteadiness for measured values very near the nominal threshold. The actuator, if it is indeed commanded to operate, runs at a preset frequency  $f$  that is determined based on open-loop control results. The responsiveness of the controller is determined by the length of time over which raw hot-film voltage measurements must be accumulated for the necessary statistics (mean of dissipated power, in this case) to converge. This time interval is typically a function of the flow time scale, but in all the experiments reported here, it was set to 0.1 s (10 to 45 flow time scales, depending on  $Re$ ). The processed value is held over this interval, while a running sum of the raw sensor signal is accumulated. At the end of each interval, the processed value is refreshed, and the running sum is reset to 0.

On/off control is demonstrated at  $Re = 0.25 \times 10^6$  and  $\alpha = 14^\circ$  using an actuation frequency of  $F^+ = 2.5$ . At this open-loop control frequency the change in hot-film signal between separated and attached flow is measurable, but quite small (0.1 mW) (see Figure 13b). Hysteresis effects are significant in this flow regime, meaning that once flow is attached by actuation it can remain attached for some time even with the actuator switched off. These effects have been exploited for purposes of power saving (Benard *et al.* 2010a). Hysteresis effects are observed for  $\alpha = 13\text{--}15^\circ$  with the NACA 0015 depending on  $Re$ . In the hysteresis regime it is advantageous to temporarily turn the actuator off to conserve power and then re-initiate the plasma when the flow is once again beginning to separate. This behavior is achieved with the on/off controller, as demonstrated in Figure 18. The dSpace controller clock is running at 50 kHz, so that the raw sensor voltage is sampled at this rate and the decision step (Step 1 in Figure 17) is performed in  $20 \mu\text{s}$ . The sensing and its online processing are initiated before time  $t = 0$  on the graph. When the controller is activated at  $t = 1.5$  s, this processed measurement is found to be above the dead zone, and the actuator is enabled within  $20 \mu\text{s}$ . The flow gets attached within the next 0.2 s, and sensing the corresponding drop in the dissipated power, the controller switches off the actuator (indicated by the flat-lining pulser input signal). From  $t = 1.5$  s to 2.75 s, the hysteresis effect causes the flow to remain attached, which is continuously verified by the controller. The flow starts to separate again at  $t = 2.75$  s, at which time the controller turns the actuator on to keep the flow attached to the airfoil, and the cycle is repeated. This behavior is consistent with the control mechanism observed in Figure 13 (i.e. transition).

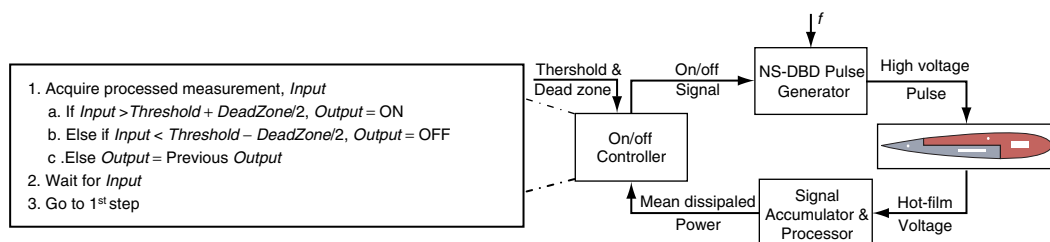


Figure 17. The on/off control scheme.

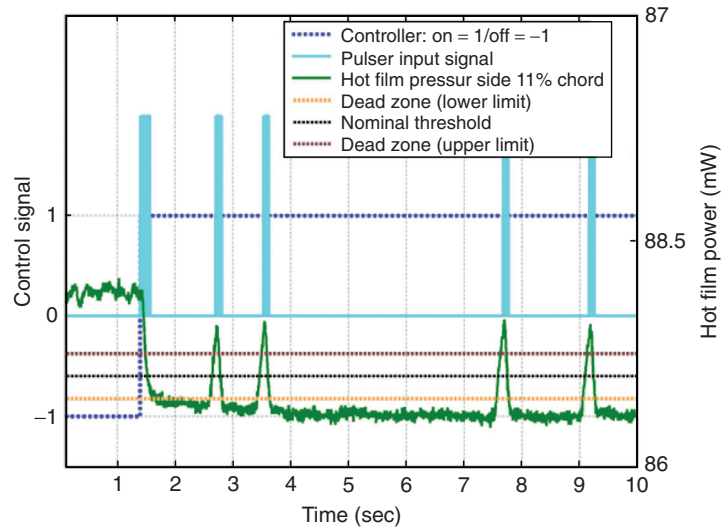


Figure 18. On/off NS-DBD controller at  $Re = 0.25 \times 10^6$ ,  $\alpha = 14^\circ$ ,  $F^+ = 2.5$ .

When the on/off controller is operated outside of the range where hysteresis effects are present (high  $\alpha$ ), the plasma must continuously run at the preset frequency to keep the flow attached (Figure 19). If the actuator switches on and off repeatedly, then the resulting disruption to the coherent vortex pattern (see Figure 15) creates large unsteady forces on the airfoil that are quite apparent to the wind tunnel operators from vibration and noise. Therefore, the threshold for the on/off controller is intentionally set low to demonstrate a proof of concept for these flow conditions. The controller deems the flow to be separated at all times, and the actuator remains enabled until the controller is manually disabled. In this case the change in the hot film signal between separated and attached flow is  $\sim 1$  mW due to higher velocity. A better illustration of this controller would be realized for dynamically changing  $\alpha$ , but the wind tunnel facility does not have this capability. For clarity the nanosecond pulser signal is not included in Figure 19 because it is operating at the predetermined frequency of  $F^+ = 2.75$  whenever the controller is enabled.

Although closed-loop control using a very simple on/off controller is successful, several issues have been encountered. Attempts to characterize the hot film signal for both baseline and open-loop control conditions have been met with limited success especially at high  $\alpha$  post-stall conditions (Figures 10, 13–14). The most problematic issue is a slow drift of the hot film signal over extended periods of constant flow conditions resulting in controller inconsistency. The reason for this drift is unknown as it

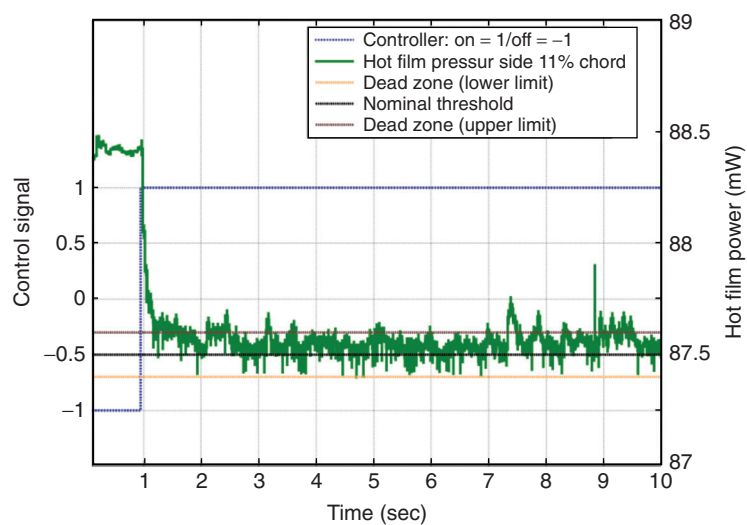


Figure 19. On/off controller at  $Re = 1.15 \times 10^6$ ,  $\alpha = 20^\circ$ ,  $F^+ = 2.75$ .

occurs regardless of whether the plasma is on or off and persists throughout the testing. This is especially problematic since the sensitivity of the hot film to  $C_L$  changes at  $x/c = 11\%$  is quite small. Consequently, the threshold had to be manually set for each control run, although the dead zone width could be retained constant. One idea for improvement, which has not been implemented yet, is to use two hot film sensors, one at the present location, and another further downstream on the pressure side. Assuming that the drift in their values are similar, one could then perform the decision-making based on the difference of the two signals. These inconsistencies motivated testing of another type of controller which does not rely on predetermined thresholds for performance.

Design and implementation of an extremum seeking controller is deemed appropriate by considering the theoretical  $C_F$  distribution (Figure 11) and the general trend that lower hot film values correspond to higher lift. This controller searches for an extremum (in this case a minimum) in the performance objective by continuously adjusting a chosen parameter of the actuation. The extremum-seeking controller is based on the Modified Nelder-Mead Algorithm implemented previously in a high Reynolds number high-speed jet forced with localized arc filament plasma actuators (Sinha *et al.* 2010). In brief, after each update of the actuation parameter of interest, the measured change in the performance objective is used to decide the sign and magnitude of the next update. In the present implementation, the objective is to keep  $C_L$  maximized by optimizing the forcing frequency of the NS-DBD plasma actuator, even when the flow speed is dynamically varied. Since  $C_L$  cannot be measured in real-time, one has to improvise with the surrogate objective of minimizing the power dissipated by the leading edge hot film sensor. However, it is shown in Figures 10 and 14 that the minimum of this quantity does not necessarily correspond directly to the minimum of the  $C_p$  value near the leading edge. This means that although using the extremum-seeking controller with the hot films may result in an increase in  $C_L$  compared to the baseline case, one cannot guarantee convergence to the optimal forcing frequency determined from the open-loop frequency sweep. The hot film data also shows that, in the range of control frequencies explored, there are several local minima and areas of relatively flat frequency response. This leads to inconsistency in the extremum-seeking controller because it is difficult for it to navigate through these frequency ranges.

The performance of the extremum-seeking controller is shown in Figures 20 and 21. In these cases, the angle of attack is held at  $18^\circ$  and the Reynolds number is varied during the run from  $Re = 0.25 \times 10^6$  to  $Re = 1.15 \times 10^6$  and back. These changes occurred over a time period of 90 seconds which is determined by the responsiveness of the wind tunnel control system. It should be noted that separation control via boundary layer transition has not been observed at this angle of attack and a preferred frequency exists in the  $C_p$  sweep data at these conditions (see Figure 14b). Figures 20 and 21 correspond to two consecutive runs with the same controller parameters and flow conditions. The extremum-seeking controller is unable to produce repeatable results, presumably due to the limited sensitivity of the hot film at its present location. In both runs, at a time of approximately 350 seconds the controller loses control authority as a result of a spike in the actuation frequency. In Figure 21, the controller is able to navigate through this spike and ultimately settle upon the optimal forcing

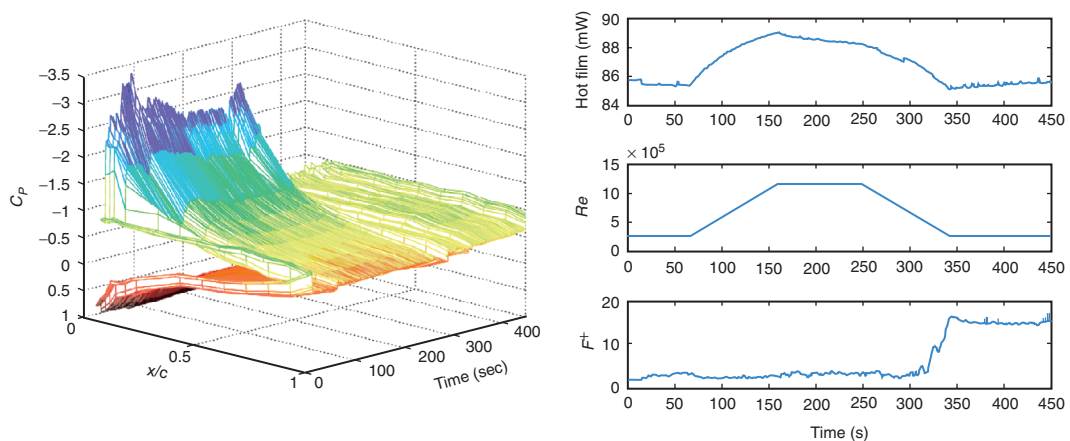


Figure 20. Extremum-seeking control:  $Re$  varied from  $0.25 \times 10^6$  to  $1.15 \times 10^6$  to  $0.25 \times 10^6$ ,  $\alpha = 18^\circ$ .

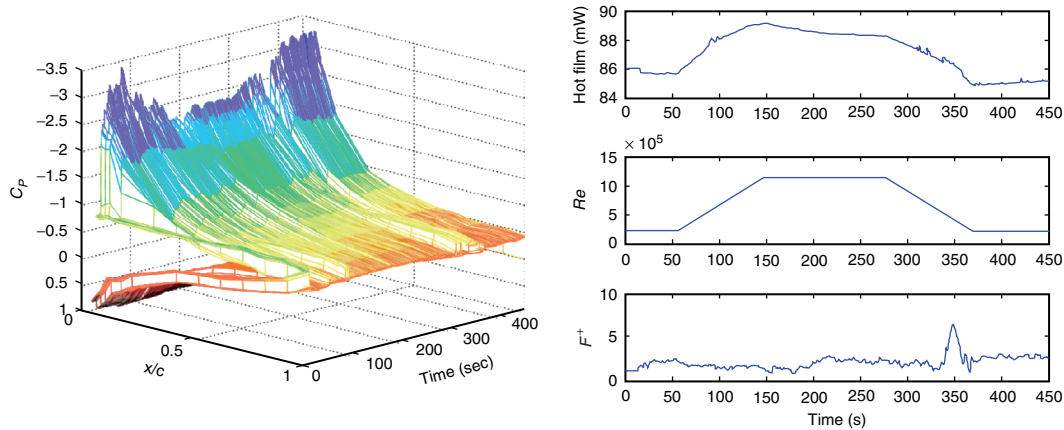


Figure 21. Performance of extremum-seeking control during a different run using the same parameters as in Figure 20.

frequency, but in Figure 20 the controller continues forcing at a frequency which is too high. We postulate that if the hot film sensor used for closed-loop control could be placed upstream of the stagnation line in the region of large  $C_F$  gradient, the consistency of the controllers would be substantially improved (see Figure 11). This has been previously shown with sensors located at  $x/c = 0.17\%$  (Poggio *et al.* 2010). In our experiments, this is not possible due to the location of the actuator recess, which is designed to provide more than adequate spacing between the hot films and electrodes to prevent equipment damage. If these fragile sensors were mounted on the dielectric even away from the electrodes they would be irrevocably damaged by physically changing the actuator.

#### 4. CONCLUSIONS

This work presents continued development and use of dielectric barrier discharge (DBD) plasma actuators driven by repetitive nanosecond pulses (NS-DBD) for high Reynolds and Mach number aerodynamic flow control. Leading edge separation control on an 8-inch chord NACA 0015 airfoil is demonstrated at various post-stall angles of attack ( $\alpha$ ) for Reynolds numbers ( $Re$ ) and Mach numbers ( $M$ ) up to  $1.15 \times 10^6$  and 0.26 respectively ( $U_\infty = 93$  m/s). The control mechanism of the NS-DBD actuators, excitation of shear layer instabilities, is believed to stem from rapid localized heating of fluid near the surface of the actuator. This is in contrast to AC-DBD actuators which function through EHD effects. The signature of this localized heating is a compression wave that propagates into the flow with each pulse. Two control mechanisms are found, depending upon  $Re$  and  $\alpha$ . At low  $Re$  ( $0.25 \times 10^6$ ) and angles of attack near stall, the NS-DBD actuator acts as an active boundary layer trip. At higher flow speeds ( $Re = 1.15 \times 10^6$ ,  $M = 0.26$ ) and angles of attack ( $\alpha > 16^\circ$ ), the NS-DBD plasma actuator excites natural flow instabilities that develop into large coherent structures. These structures increase the momentum in the near-wall fluid by entraining it from the freestream. The efficacy of this control mechanism is dependent on the frequency of actuation with best results obtained around  $F^+ \approx 2$ . This mechanism is widespread in the literature and has been successful on various aerodynamic systems with multiple actuation techniques. A brief comparison with the more common AC-DBD plasma actuation is presented to demonstrate the difference in control authority over a range of  $Re$ . The AC-DBD and NS-DBD actuators have similar control authority at  $Re = 0.25 \times 10^6$ . The NS-DBD actuator maintains very similar control authority up to the maximum  $Re$  tested ( $1.15 \times 10^6$ ), but the control authority of the AC-DBD plasma actuator decreases as  $Re$  is increased with effectively zero control authority at or above  $Re = 0.75 \times 10^6$ .

NS-DBD plasma actuators are used in conjunction with a surface-mounted hot film and constant voltage anemometer for two closed-loop control strategies. The controller uses the mean power dissipated by a hot film on the pressure side of the airfoil near the leading edge ( $x/c = 11\%$ ) to estimate relative  $C_L$  in real-time. The hot film is sensitive to changes in the stagnation line location which correlates with  $C_p$  distribution on the airfoil and subsequently  $C_L$ . This controller is most useful at low  $Re$  and moderate  $\alpha$ . In this regime, the control mechanism is an active boundary layer trip. The logic allows the controller to turn off the plasma for periods of time where hysteresis effects keep the flow

attached to the airfoil, thereby reducing power consumption. The on/off controller is also used in flow conditions where the flow instabilities are excited (high  $Re$ , high  $\alpha$ ). In this regime the actuator must constantly remain active to avoid high unsteady loading on the airfoil. Extremum-seeking control is used to optimize the forcing frequency of the actuator during dynamic variation of  $Re$  by minimizing the mean hot film signal. Extremum seeking controller performance is not consistent presumably due to sub-optimal hot film sensor location which should be upstream of stagnation on the airfoil pressure side for best results. Although the full utility of the controllers is not realized in this work, several challenges typically associated with integration of DBD plasma actuators into a feedback control system have been overcome. The most important of these is the demonstration of control authority at typical aircraft takeoff and landing Mach numbers.

## ACKNOWLEDGMENTS

This work was funded in part by the Air Force Research Laboratory Air Vehicles Directorate with Dr. Jonathan Poggie. Additional funding was provided by the Ohio State University. Two undergraduate students, Chris Wiet and Troy Niekamp, were very helpful in this work and their help is appreciated. The authors would also like to thank Tao Systems for assistance with hot film setup and installation.

## REFERENCES

- Adrian, R., Christensen, K. and Liu, Z. (2000) Analysis and interpretation of instantaneous turbulent velocity fields. *Experiments in Fluids*, Vol. 29: 275–290.
- Becker R, King R, Petz R, Nitsche W (2007) Adaptive Closed-Loop Separation Control on a High-Lift Configuration Using Extremum Seeking. *AIAA Journal* 45[6]: 1382–1392.
- Benard N, Bonnet JP, Moreau E, Griffin J, Cattafesta LN, III (2010a) On the Benefits of Hysteresis Effects for Closed-Loop Separation Control Using Plasma Actuation. *AIAA Paper* 2010–4259.
- Benard N, Moreau E, Griffin J, Cattafesta L (2010b) Slope Seeking for Autonomous Lift Improvement by Plasma Surface Discharge. *Experiments in Fluids* 48: 791–808.
- Corke TC, Post ML, Orlov DM (2009) Single Dielectric Barrier Discharge Plasma Enhanced Aerodynamics: Physics, Modeling and Applications. *Experiments in Fluids* 46[1]: 1–26.
- Forte M, Jolibois J, Pons J, Moreau E, Touchard G, Cazalens M (2007) Optimization of a Dielectric Barrier Discharge Actuator by Stationary and Non-Stationary Measurements of the Induced Flow Velocity: Application to Airflow Control. *AIAA Journal* 43: 917–928.
- Gaitonde DV, Samimy M (2011) Coherent structures in plasma-actuator controlled supersonic jets: Axisymmetric and mixed azimuthal modes. *Physics of Fluids* Vol. 23, pp. 095104–1 to 095104.
- Glezer A, Amitay M (2002) Synthetic Jets. *Annual Review of Fluid Mechanics* 34: 503–529.
- Greenblatt D, Wygnanski IJ (2000) The control of flow separation by periodic excitation. *Progress in Aerospace Sciences* 36[7]: 487–545.
- Kelley, C, Bowles, P, Cooney, J, He, C, Corke, T, Osborne, B, Silkey, J and Zehnle, J (2012) High Mach Number Leading-edge Flow Separation Control using AC DBD Plasma Actuators. *AIAA Paper* 2012–0906.
- Little, J, Takashima, K, Nishihara, M, Adamovich, I and Samimy, M (2010) High Lift Airfoil Leading Edge Separation Control with Nanosecond Pulse Driven DBD Plasma Actuators. *AIAA Paper* 2010–4256.
- Little J, Takashima K, Nishihara M, Adamovich I, Samimy M (2012) Separation Control with Nanosecond Pulse Driven Dielectric Barrier Discharge Plasma Actuators. *AIAA Journal* 50[2]: 350–365.
- Macheret SO, Shneider MN, Miles RB (2004) Magnetohydrodynamic and Electrohydrodynamic Control of Hypersonic Flows of Weakly Ionized Plasmas. *AIAA Journal* 42[7]: 1378–1387.
- McLean J, Crouch J, Stoner R, Sakurai S, Seidel G, Feifel W, Rush H (1999) Study of the Application of Separation Control by Unsteady Excitation to Civil Transport Aircraft. In: NASA CR.
- Moreau E (2007) Airflow control by non-thermal plasma actuators. *Journal of Physics D: Applied Physics* 40[3]: 605–636.
- Patel MP, Sowle ZH, Corke TC, He C (2007) Autonomous Sensing and Control of Wing Stall Using a

- Smart Plasma Slat. *Journal of Aircraft* 44[2]: 516–527.
- Patel, M., Ng, T., Vasudevan, S., Corke, T., Post, M., McLaughlin, T. and Suchomel, C. (2008) Scaling Effects of an Aerodynamic Plasma Actuator. *Journal of Aircraft* 45 [1]: 223–236.
- Pinier JT, Ausseur JM, Glauser MN, Higuchi H (2007) Proportional Closed-Loop Feedback Control of Flow Separation. *AIAA Journal* 45[1]: 181–190.
- Poggie J, Tillman C, Flick P, Silkey J, Osborne B, Ervin G, Maric D, Mangalam S, Mangalam A (2010) Closed-Loop Stall Control System. *Journal of Aircraft* 47[5]: 1747–1755.
- Roupassov D, Nikipelov A, Nudnova M, Starikovskii A (2009) Flow Separation Control by Plasma Actuator with Nanosecond Pulsed-Periodic Discharge. *AIAA Journal* 47[1]: 168–185.
- Samimy M, Debiasi M, Caraballo E, Serrani A, Yuan X, Little J, Myatt JH (2007) Feedback control of subsonic cavity flows using reduced-order models. *Journal of Fluid Mechanics* 579: 315–346.
- Samimy M, Kim J-H, Kearney-Fischer M, Sinha A (2010) Acoustic and Flow Fields of an Excited High Reynolds Number Axisymmetric Supersonic Jet. *Journal of Fluid Mechanics* 656: 507–529.
- Seifert A, Darabi A, Wagnanski I (1996) Delay of Airfoil Stall by Periodic Excitation. *Journal of Aircraft* 33[4]: 691–698.
- Sinha A, Kim K, Kim J, Serrani A, Samimy M (2010) Extremizing Feedback Control of a High-Speed and High Reynolds Number Jet. *AIAA Journal* 48[2]: 387–399.
- Takashima K, Zuzek Y, Lempert WR, Adamovich IV (2011) Characterization of Surface Dielectric Barrier Discharge Plasma Sustained by Repetitive Nanosecond Pulses. *Plasma Sources Science and Technology* 20: 055009.
- Thomas F, Corke T, Iqbal M, Kozlov A, Schatzman D (2009) Optimization of Dielectric Barrier Discharge Plasma Actuators for Active Aerodynamic Flow Control. *AIAA Journal* 47[9]: 2169–2178.